

# Impact of different microphysics and cumulus parameterizations in WRF for heavy rainfall simulations in the central segment of the Tianshan Mountains, China



Yang Liu<sup>a,b,c,d</sup>, Xi Chen<sup>c</sup>, Qian Li<sup>a,b,c,d</sup>, Jinming Yang<sup>b</sup>, Lanhai Li<sup>a,b,c,d,\*</sup>, Tingting Wang<sup>e</sup>

<sup>a</sup> State Key Laboratory of Desert and Oasis Ecology, Xinjiang Institute of Ecology and Geography, Chinese Academy of Sciences, Urumqi 830011, China

<sup>b</sup> Ili Station for Watershed Ecosystem Research, Chinese Academy of Sciences, Xinyuan 835800, China

<sup>c</sup> Research Center for Ecology and Environment of Central Asia, Chinese Academy of Sciences, Urumqi 830011, China

<sup>d</sup> University of Chinese Academy of Sciences, Beijing 100049, China

<sup>e</sup> Foreign Affairs Office of Xinjiang Uygur Autonomous Region, People's Government of Xinjiang Uygur Autonomous Region, Urumqi 830000, China

## ARTICLE INFO

### Keywords:

WRF  
Heavy rainfall  
Microphysics scheme  
Cumulus convection scheme  
Tianshan mountains

## ABSTRACT

With the continuous deepening of hydrological simulations in the alpine regions, high-resolution rainfall data is urgently needed as driving data for distributed hydrological models. Therefore, the objective of this study is to evaluate the performance of the WRF model for the accumulated rainfall simulations in the central segment of the Tianshan Mountains. The WRF model is configured with triple nesting of 27, 9, and 3 km for 28 experimental setups using four microphysics schemes (Morrison, WSM6, Goddard, and Thompson) and seven cumulus convection schemes (Kain-Fritsch, Betts-Miller-Janjic, Grell-Freitas, Grell-3, KF-CuP, New SAS, and Grell-Dévényi). The performance of these WRF configurations for two typical heavy rainfall simulations are first assessed via comparisons between simulation and observation; then, its influence on the simulations is analyzed. The results show that 1) There are significant differences in the rainfall area simulated by 28 combinations; 2) The 28 experimental setups show that higher snow crystal content is consistent with more rainfalls. Only the WSM6 possesses the mechanism to adjust snow and ice content with the temperature, serving as the most suitable microphysics scheme for rainfall simulation; 3) From the perspective of the accumulated rainfall and its large value distribution, the advantage of the Grell-3 possesses the mechanism for the settlement effect extended to adjacent grids, making it the most suitable cumulus convection scheme for the simulation. Overall, the WRF model presents a strong capacity for rainfall simulation in complex terrain. Statistical investigations on various WRF setups identify suitable microphysics and cumulus convection schemes to predict heavy rainfall in the Tianshan Mountains accurately.

## 1. Introduction

Heavy rainfall (HR) is common in disastrous weather conditions around the world, especially in mountainous areas (Khodayar et al., 2018; Chen et al., 2019). HR is characterized by its sudden occurrence, large amount of rain, and uneven spatial and temporal distribution (Nikolopoulos et al., 2010). As initiators for various severe hazards such as flash floods, landslides, debris flows, and glacial lake outbursts, HR affects our society on a large scale (Reder et al., 2018). From the perspective of climatology, HR is from the interactions between various weather system scales with macro- and microphysical processes (Hoose et al., 2018). Therefore, the quantitative precipitation forecast of heavy

rainfall in mountainous regions is conducive to rainfall-induced disaster prevention and reduction (Piciullo et al., 2018).

In recent years, numerical weather predictions for rainfall forecast have been widely researched in a wide range of atmospheric sciences (Patel et al., 2019; Pennelly et al., 2014; Li et al., 2019a, b, c). Among all kinds of mesoscale numerical weather prediction models, Weather Research and Forecasting (WRF) is one of the most welcomed, cutting-edge models with various physical schemes that facilitates the prediction of weather variables with high accuracy (Scaff et al., 2019; Hasan and Islam, 2018; Avolio and Federico, 2018). Previous studies have demonstrated that the top two physics schemes are microphysics and cumulus convection parameterization schemes, with the precipitation

\* Corresponding author at: State Key Laboratory of Desert and Oasis Ecology, Xinjiang Institute of Ecology and Geography, Chinese Academy of Sciences, Urumqi 830011, China.

E-mail address: [lilh@ms.xjb.ac.cn](mailto:lilh@ms.xjb.ac.cn) (L. Li).

simulation is less sensitive to microphysics in contrast to cumulus convection scheme (Liu et al., 2018a, b, c; Nasrollahi et al., 2012). Jankov et al. (2005) investigated different integrations of cumulus convection schemes, microphysics schemes, and boundary conditions, finding no significant improvement in any configuration. Additionally, the impact of cumulus convection scheme on precipitation pattern simulations was also validated by Gallus (1999) and Wang and Seaman (1997). In a recent study, Tian et al. (2017) researched various physical schemes, arguing that the precipitation amounts and patterns varied with microphysics and cumulus convection schemes in semi-humid and semi-arid areas. Generally, microphysics and cumulus convection schemes are empirical treatment methods based on limited observation and imperfect theories. Furthermore, various precipitation intensity and ranges in various precipitation systems are from different convection factors.

Each physical scheme is tailored to certain physical processes with distinctive features (Efstathiou et al., 2013; Dasari and Salgado, 2015). Since the WRF model was released, various integrations of microphysics and cumulus convection schemes have been researched and used globally to conduct rainfall simulations (Politi et al., 2018; Tian et al., 2017; Liu et al., 2012), for example, in Africa (Diaz et al., 2015), Europe (Banks and Baldasano, 2016), North America (Burakowski et al., 2016), and Asia (Cannon et al., 2017). Previous studies have shown that atmospheric heat and moisture tendencies are provided by microphysics scheme, demonstrating the vertical flux of the precipitation and sedimentation processes (Sikder and Hossain, 2016; Tiwari et al., 2018a, b). In contrast to the microphysics schemes, cumulus convection schemes vertically redistributes heat and moisture, which are immune to latent heating due to precipitation (Cai et al., 2018; Huang and Gao, 2017; Budakoti et al., 2019). The impact of different microphysics schemes have been investigated by several studies. For example, for the precipitation event that occurred over the Western Himalayas in June 2013, the Goddard scheme made a sufficient simulation for features of the local-scale precipitation (Chawla et al., 2018). For the rainfall event in Pakistan during 26–30 July 2010, the influence of topography on rainfall events was evaluated by the Morrison scheme, illustrating the heterogeneity features of rainfall distribution (Muhammad Tahir et al., 2015). In China, Thompson and WRF Single-Moment 6 (WSM6) are widely used as common microphysics schemes, while Thompson is fell short of efficiency in convective rainfall regions. The WSM6 performed better in relation to the rainfall observations (Huang et al., 2020; Tian et al., 2017; Kim et al., 2013). Additionally, the role of cumulus convection scheme on climate projection has been studied. In the United States, the Kain-Fritsch (KF) scheme displays better performance in contrast to Betts-Miller-Janjic (BMJ); it inclines to overrate light rain events compared with BMJ (Wang and Seaman, 1997). Mugume et al. (2017) reported that the Grell-Freitas (GF) scheme outweighs the BMJ and KF schemes in rainfall simulation due to overestimation. These studies highlighted that there are mechanism differences in microphysics and cumulus convection schemes with various vertical structures. Eventually, it can be inferred that the simulations of microphysics and cumulus convection schemes suitable to other alpine regions may not be compatible with the Tianshan Mountains.

The Tianshan Mountains are known as the “water tower” of Central Asia due to its annual rainfall of around 300 mm/year to 900 mm/year (Yang et al., 2014). Located in the hinterlands of Eurasia, the Tianshan Mountains are far from the ocean, with a temperate continental climate free from monsoons (Liu et al., 2018a, b, c). Due to the adverse effects from the transfer of water vapor over long distances and the terrain barrier, the rainfall features are similar to those of inland mountains, which are dominated by large-scale weather systems (Yao et al., 2018). With low frequencies and large amounts, the rainfall distribution presents obvious spatial heterogeneity with short spatio-temporal patterns (Li et al., 2019a, b, c). Thus, HR simulation over the region is a challenging task, especially for the alpine areas. The WRF model was also implemented to simulate HR with different physical schemes in order to

tap into the dependence on physical schemes, which are followed by the examination of forming mechanisms, developing processes, fall zones, and rainfall amounts (Navale et al., 2020; Yu et al., 2011; Zhou and Mu, 2018; Zhang et al., 2017). These results indicate that the integration of microphysics and cumulus convection schemes are quite significant for rainfall investigation. For instance, HRs present obvious heterogeneity in the temporal and spatial distributions in mountainous regions due to the complexity and uncertainty of atmospheric processes influenced by topographical conditions such as altitude, slope, and aspect (Xu et al., 2018; Pontoppidan et al., 2017). Indeed the significant differences in land cover at different phases produce more uncertainty about simulation (Miao et al., 2018); there have been no explicit assessments for cloud-resolving scales (< 5 km) due to inadequate field observations. By the same token, microphysics and cumulus convection schemes have not been comprehensively studied to overcome the limitations imposed by the HR features of the complicated landform. Therefore, precipitation simulations with high resolutions in the Tianshan Mountains could be optimized in numerical models.

In this study, two HRs are investigated by WRF-ARW (v3.9) model in the central Tianshan Mountains, both of which had been destructive events. The study aims at clarifying the capability of WRF to reproduce the HRs and the sensitivity with four microphysics and seven cumulus convection schemes. Furthermore, the hydrometeor distribution in WRF performance is investigated thoroughly. As for meso- and micro-scale dynamical mechanisms in interactions of atmosphere and underlying complex landform, the model output of the most suitable WRF running at a convection-permitting scale (3-km spatial resolution) is studied.

## 2. Methodology

### 2.1. Description of the study area

The largest mountains in Central Asia, the Tianshan Mountains, start from the Kyzylkum Desert of Uzbekistan, enter Xinjiang, straddle Tajikistan, Kazakhstan, and Kyrgyzstan, and gradually integrate into Gobi, east of Hami of China. A complex terrain with an average altitude of about 4000 m exists in the mountainous region, with the highest peak, Tomor, at 7435.3 m. The transverse length from east to west is more than 2500 km; the width from north to south is approximately 250–350 km (Li et al., 2018). The central segment of the Tianshan Mountains are composed of a series of mountain ranges, mountain basins, valleys, pre-mountain plains, and other geomorphological units (Fig. 1).

The Tianshan Mountains trap a large amount of Atlantic moisture from the westerly circulation due to vast mountain massif, unique geographical location, and the northern mountains' strong latitudinal circulation. Therefore, the rainfall zone of Tianshan Mountains is usually formed during the summer with huge differences in rainfall in various regions (Yang et al., 2014).

Tianshan Mountains are known as the “water tower” of Central Asia, as well as the “wet island” in arid areas of northwest China. Glaciers, permanent snow, and other water resources are abundant in this mountainous area. Many rivers, such as the Tarim River (the longest inland river in China) and the Ili River (an inland river with the largest water volume in Xinjiang), originate from this area (Liu et al., 2018a, b, c).

### 2.2. WRF model set-up

The present study uses the WRF-ARW (v3.9) model. In this study, the model is configured with three nested grid domains consisting of 27-km ( $200 \times 200$ ), 9-km ( $202 \times 202$ ), and 3-km ( $226 \times 226$ ) horizontal grid spacing along with 30 vertical levels. The parent domain spans from  $33.9044^\circ$  to  $135.8333^\circ$ E and from  $15.7230^\circ$  to  $67.3303^\circ$ N; the second nested domain spans from  $71.9397^\circ$  to  $98.5692^\circ$ E and from

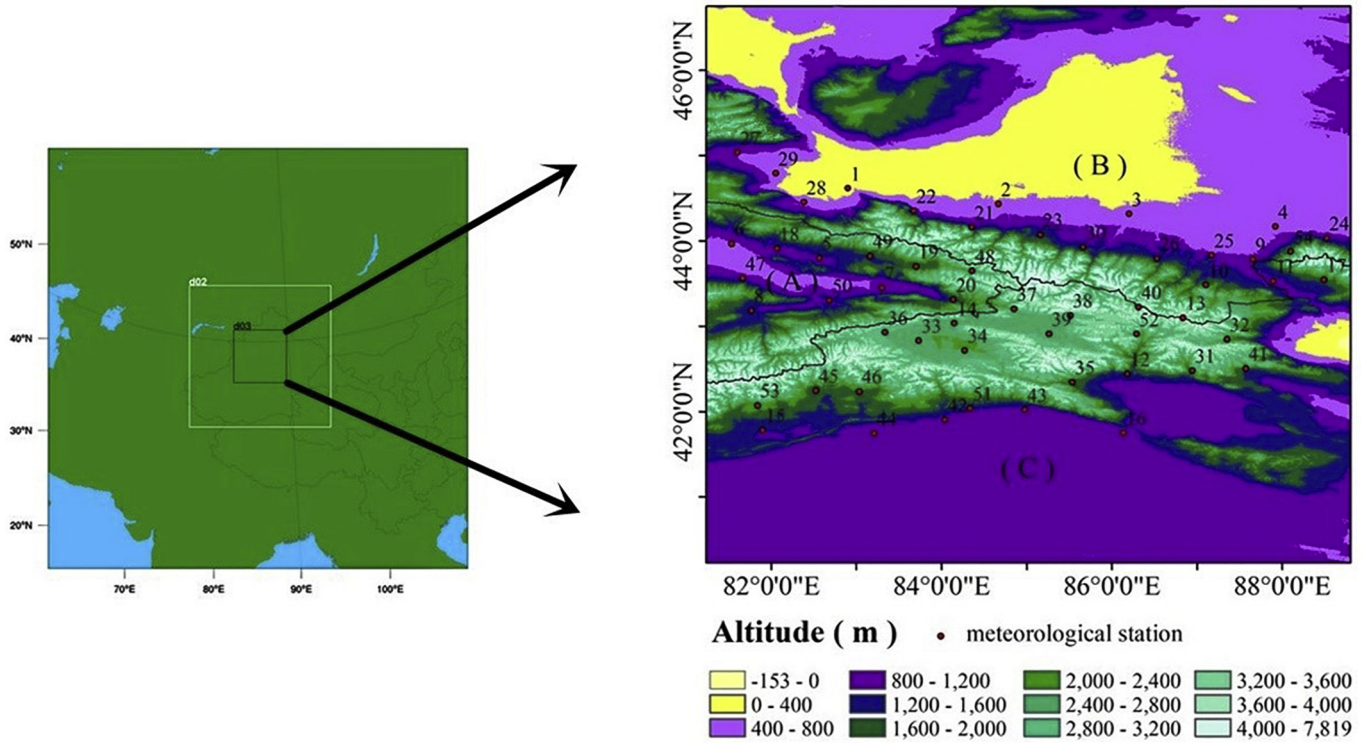


**Fig. 1.** WRF model domains - d03 innermost domain for the central segment of the Tianshan Mountains (left), and location of the selected meteorological station with available data for rainfall (right).

34.4470° to 51.6633°N; the third nested domain spans from 80.7251° to 89.7947°E and from 40.0882° to 46.4210°N.

The initial and boundary conditions for the WRF simulations are derived from the six-hourly global reanalysis data provided by the  $1^\circ \times 1^\circ$  grids of the NCEP Final (FNL) operational model. The time step of the WRF model is set to be 18 s, which equates to  $6 \times dx$  (in km);  $dx$  is the grid spacing of the innermost domain (Hou et al., 2015). The output frequency of the WRF model is 1 h. In tests, the spin-up time within 12–24 h has little effect on the HRs simulation in this study. Thus, the spin-up period of 12 h is used to develop smaller-scale convective features, contributing to an accurate rainfall simulation on the mesoscale regions.

Four microphysics and seven cumulus convection schemes are combined together with determined radiation and land surface scheme based on the widely used in the Introduction. The Morrison 2-moment (Morrison), WSM6, Goddard, and Thompson are chosen for micro-physics schemes, and the cumulus convection schemes comprise Kain-Fritsch(KF), Betts-Miller-Janjic (BMJ), Grell-Freitas(GF), Grell3, KF-CuP, New SAS, and Grell-Dévényi(GD), as shown in Table 1. In total, 28 combinations are designed with the selected physical schemes. Additionally, Noah is used as the LSM; SU and MYJ are chosen for PBLs; Goddard and Dudhia are used as short and long radiation schemes, respectively.

### 3. Experiment design and methods

#### 3.1. In-situ rainfall observations

Rain-gauge observations from 54 meteorological stations in the central Tianshan Mountains are used to evaluate the model results from the high-resolution domain ( $3 \times 3$  km). The observation data from the meteorological sites are from the China Meteorology Administration. In the comparison of the simulations and observations, the inverse distance weight interpolation method is applied to the grid point at the innermost domain that is spatially closest to each rain-gauge location;

**Table 1**  
WRF Experiment details for simulations.

Member	Cumulus parameterization	Microphysics
Case 1	Kain-Fritsch	Morrison
Case 2	Kain-Fritsch	WSM6
Case 3	Kain-Fritsch	Goddard
Case 4	Kain-Fritsch	Thompson
Case 5	Betts-Miller-Janjic	Morrison
Case 6	Betts-Miller-Janjic	WSM6
Case 7	Betts-Miller-Janjic	Goddard
Case 8	Betts-Miller-Janjic	Thompson
Case 9	Grell-Freitas	Morrison
Case 10	Grell-Freitas	WSM6
Case 11	Grell-Freitas	Goddard
Case 12	Grell-Freitas	Thompson
Case 13	Grell3	Morrison
Case 14	Grell3	WSM6
Case 15	Grell3	Goddard
Case 16	Grell3	Thompson
Case 17	KF-CuP	Morrison
Case 18	KF-CuP	WSM6
Case 19	KF-CuP	Goddard
Case 20	KF-CuP	Thompson
Case 21	New SAS	Morrison
Case 22	New SAS	WSM6
Case 23	New SAS	Goddard
Case 24	New SAS	Thompson
Case 25	Grell-Dévényi	Morrison
Case 26	Grell-Dévényi	WSM6
Case 27	Grell-Dévényi	Goddard
Case 28	Grell-Dévényi	Thompson

the simulation of accumulated rainfall amounts is compared with the actual amounts for a simpler and more straightforward approach.

The main purpose of the comparison is to explore the behaviors and differences between the 28 combinations.



Fig. 2. Spatial values of the seven categorical indices for two HRs with the 28 members of the physical combination.

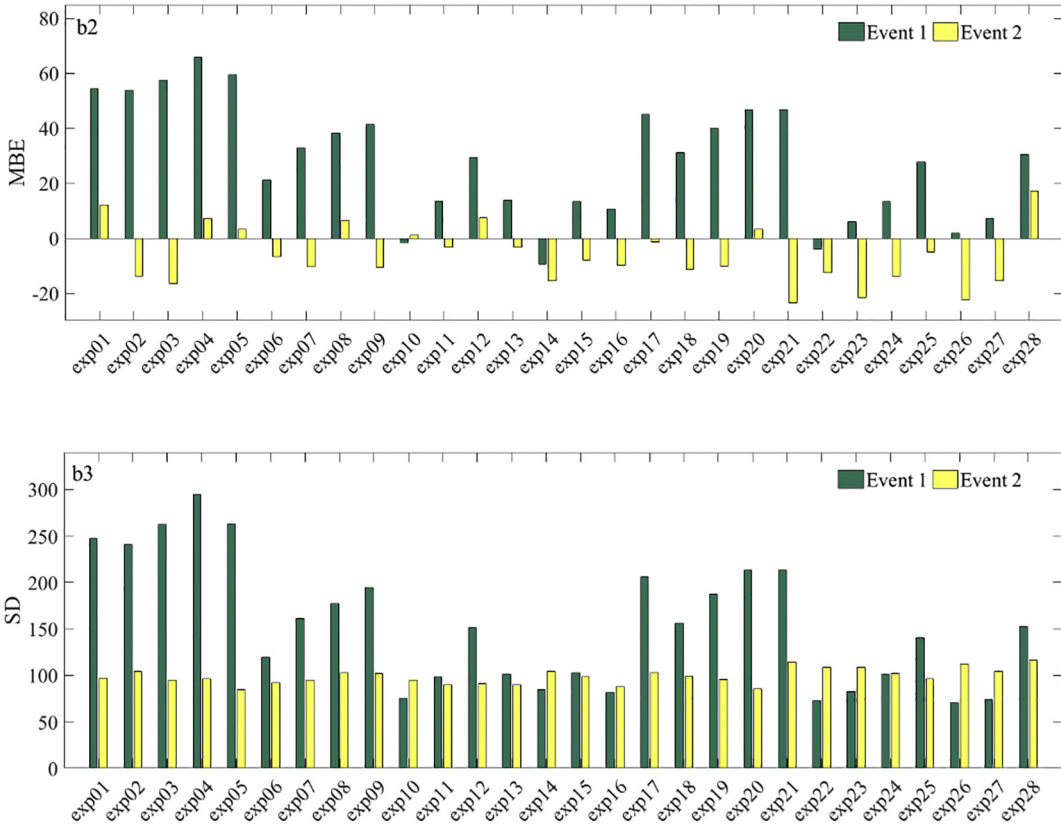


Fig. 2. (continued)

### 3.2. Meteorological characterization of rainfall events

The selection of two rainfall events are frontal system, representing the region. A sharp fall in temperature and heavy rainfall in high elevations (above 1000 m), coupled with strong winds characterized the heavy rainfalls.

#### 3.2.1. 15–20 May 2015, heavy rainfall event (MAY15)

From 15 to 20 May 2015, the Eurasian west wind brings low troughs to Xinjiang, with HR in the north. A heavy rainfall occurred in the Ili Valley and the central Tianshan Mountains. From 17 May 2015 12:00 UTC to 20 May 2015 00:00 UTC, heavy rainfall occurred with cumulative rainfall amounts at 19 stations exceeding 24.0 mm.

#### 3.2.2. 26–28 June 2015, heavy rainfall event (JUNE26)

Air flows from the Arabian Sea arrived in the western part of Xinjiang, bringing low-latitude moisture to the interior of the Central Asian vortex before moving to Xinjiang for two days. There was heavy rainfall that occurred along the Tianshan Mountains from 26 to 28 June 2015. Most of the rainfall was occurred from 26 June 2015 12:00 UTC to 28 June 2015 18:00 UTC, with accumulation at 18 stations exceeding 24.0 mm.

### 3.3. Verification strategy

The WRF model performance is evaluated by examining the temporal and spatial agreement between simulation and observation. In this study, categorical statistics are employed, which comprise the critical success index (CSI), probability of detection (POD), and false alarm ratio (FAR); these are also used to verify the WRF model's performance in simulating rain/no rain events at different thresholds. Rainfall amounts below 0.2 mm are considered as no rain in this study, following Schirmer and Jamieson (2015). The calculation formulas are as follows:

$$CSI_k = \frac{NA_k}{NA_k + NB_k + NC_k} \times 100\% \quad (1)$$

$$POD_k = \frac{NA_k}{NA_k + NC_k} \times 100\% \quad (2)$$

$$FAR_k = \frac{NA_k}{NA_k + NB_k} \times 100\% \quad (3)$$

The above formulas are CSI, FAR, and POD.  $NA_k$  is the number of stations with correct forecasts,  $NB_k$  is the number of stations with false alarms, and  $NC_k$  is the number of stations with missing alarms. In these formulas,  $k$  is used to distinguish the two selected HRs.

Meanwhile, the evaluation is performed using the root mean square error (RMSE), the mean bias error (MBE), and standard deviation (SD) to describe the deviation between the simulation and observation.

$$RMSE = \frac{\sqrt{\frac{1}{n} \sum_{i=1}^n (M_i - O_i)^2}}{\frac{1}{n} \sum_{i=1}^n O_i} \times 100\% \quad (4)$$

$$MBE = \frac{\frac{1}{n} \sum_{i=1}^n (M_i - O_i)}{\frac{1}{n} \sum_{i=1}^n O_i} \times 100\% \quad (5)$$

$$SD = \frac{\sqrt{\frac{1}{n} \sum_{i=1}^n (M_i - O_i - MBE)^2}}{\frac{1}{n} \sum_{i=1}^n O_i} \times 100\% \quad (6)$$

In these formulas,  $n$  is the number of sites used for the simulation,  $M_i$  is the simulated cumulative rainfall amount at the site, and  $O_i$  is the amount of the observed cumulative rainfall at the site. The final values of the three indices represent the mean magnitudes of the simulation error and the mean bias error (MBE), respectively. The perfect score of all three indices is 0. The final values of the indices are represented as percentages of the average in observations to compare the simulations for the cumulative rainfall amount of the two HRs.

## 4. Result

To reduce the uncertainties of the verification results, the simulation of cumulative rainfall amounts of the above two HRs are verified.

### 4.1. Scores for the two HRs

The categorical index values (1–6) for the two HRs with the 28 combinations are shown in Fig. 2.

In Fig. 2 (a1–a3), the FAR, POD, and CSI scores of the innermost domain simulations of the two HRs (MAY15 and JUNE26) are illustrated. The first is the FAR. For the 48-h rainfall, all of the FAR scores are lower than 0.32. The FAR range is 0.27–0.32 for MAY15 and 0.13–0.19 for JUNE26. Similar methods are applicable to POD, whose scores for both HRs are higher than 0.92; the POD range is 0.92–0.96 for MAY15 and 0.92–0.99 for JUNE26. The last measure is CSI, whose scores for both HRs are higher than 0.67; the CSI score range is 0.67–0.69 for MAY15 and 0.78–0.81 for JUNE26. In conclusion, there are good performances of FAR, POD and CSI for 0.02 mm/48 h thresholds in the 28 combinations for the simulation, which means that even rainfall in spatial distributions can be simulated accurately.

The RMSE, MBE, and SD of the innermost domain simulations of MAY15 and JUNE26 are scored to examine the performance of the WRF configurations (Fig. 2, b1–b3). The RMSE for both simulations is higher than 69.22; the RMSE ranges are 69.22–103.99 for MAY15 and 78.32–102.24 for JUNE26. Moreover, the MBE range is −9.38–65.81 for MAY15 and −23.58–17.22 for JUNE26. Furthermore, the SD of the two HRs are higher than 72.33: the SD is 72.33–247.34 for MAY15 and 87.85–116.82 for JUNE26.

The scores of different configurations that do not differ remarkably. Therefore, the changes between the simulations on the macroscopic scale will be explored.

### 4.2. Spatial patterns of rainfall simulation among the different combinations

The 48-h accumulated rainfall for the two HRs is simulated by the WRF with 28 experimental setups (Figs. 3–4). Certain simulations present large positive deviation in the humid western range (A zone), while certain simulations present large negative deviations in the semi-arid northern and southern ranges (B and C zones) (Fig. 5).

All 28 combinations could simulate the heavy rainfall zone in the central segment effectively (Fig. 3, a1–a28). The rainfall zone takes on an olive shape with a strong central part and weakened edge; for example, it stretches in a west-east direction. Meanwhile, the extending trend of rainfall zone in the mountain-oasis is presented in the simulation.

There is a huge difference in simulations among the 28 combinations. As for the same cumulus convection scheme, the microphysics schemes of the rainfall zone of the 48-h cumulative rainfall amount  $\geq 24.0$  mm are Morrison, Thompson, Goddard, and WSM6, in descending order. Moreover, for the same microphysics scheme, the cumulus convection schemes for the rainfall zone of 48-h cumulative rainfall amount  $\geq 24.0$  mm include KF, BMG, G-F, KF-CuP, and New SAS, in descending order. The simulated rainfall area is larger than the real area. There are false HR areas in the eastern and southern parts.

Furthermore, it is evident that the cumulative rainfall amounts simulations from the 28 combinations are close to the following meteorological stations: 1–6, 15, 17, 20, 23, 24, 27, 29, 30, 33, 41–48, 51–52, and 54 (average deviation: −8.90–5.30 mm) (Fig. 5a). Moreover, the cumulative rainfall amounts simulated by the M13–M16 and M26–M27 combinations are close to the observation at the 54 meteorological stations (the deviation range is −2.67–1.8 mm); meanwhile, there are simulations of non-existing rainfall zones in the eastern part from M1, M14–M17, M21, and M25–M27.

For JUNE26, the 28 combinations could also effectively simulate the

HR zone of the central segment (Fig. 4, b1–b28). The HR center is mainly concentrated in the western parts of the Tianshan Mountains. HR gradually weakens from west to east with a tendency of being weak on the northern and southern belt of Tianshan Mountains.

There is a significant difference in simulations among the 28 combinations. As for the same cumulus convection scheme, the 48-h simulated cumulative rainfall amount  $\geq 24.0$  mm includes Morrison, Thompson, Goddard, and WSM6, in descending order. For the same microphysics scheme, the combinations of simulated 48-h cumulative rainfall amount  $\geq 24.0$  mm include KF, BMG, G-F, KF-CuP, and New SAS, in descending order. There are false HR areas in the eastern parts.

In Fig. 5b, the cumulative rainfall amounts simulated by the 28 combinations are close to those of meteorological stations 2–4, 7, 9, 16, 19, 21–29, 33–36, 38–39, 40, 42, 43, 47, 51, and 53 (average deviation: −9.40–5.90 mm). Additionally, the cumulative rainfalls simulated by combinations M3, M14, M15, M19, and M23 are close to the observation of 54 meteorological stations (the deviation range is 1.81–5.01 mm). There are also simulations of non-existent rainfall zones in the southern and northern Tianshan Mountains in the eastern from M3, M7, M12, M14, M15, M19, M22, M23, and M27.

### 4.3. Profiles of the vertical mixing

To optimize the understanding of the hydrometeor distribution in the microphysics schemes, Fig. 6 lists the average spatio-temporal vertical profiles of the mixture ratios of rain, ice crystal, cloud water, and snow crystal within the study area. The mixing ratio of the four hydrometeors in the clouds increases accordingly with barometric pressure and then decreases.

In Fig. 6(a1–a4), there are significant differences between the vertical profiles of the hydrometeors in the microphysics scheme for every combination. The maximum cloud water mixing ratio for MAY15 is 650 hPa. With a barometric pressure layer of 650 hPa, the minimum and maximum of cloud water mixing ratios are 0.38 g/kg from Grell-3-WSM6 and 1.87 g/kg from BMJ-Morrison. The maximum cloud water mixing ratio for JUNE26 is 600 hPa. With a barometric pressure layer of 600 hPa, the minimum and maximum of cloud water mixing ratios are 3.26 g/kg from New SAS-WSM6 and 5.09 g/kg from BMJ-Morrison. As for the same cumulus convection scheme, the simulated cloud water mixing ratios of every scheme are ranked in descending order: Morrison, Thompson, Goddard, and WSM6.

Rainwater is the large-particle liquid state for convection sustainability. The rain mixing ratio on MAY15 started increasing at 850 hPa, and then reduced quickly to 750 hPa. The focus of this research is on the change in the rain mixing ratio within a range of 750–850 hPa. For the same cumulus convection scheme, the rain mixing ratio of the Morrison scheme presents slow growth with increased barometric pressure; however, the rain mixing ratio of the Goddard scheme increases rapidly with increased barometric pressure. The difference in rain mixing ratios between them is 0.12 g/kg. Additionally, the rain mixing ratio on JUNE26 increased from 650 hPa to 850 hPa, then reduced quickly to 650 hPa. The rain mixing ratio of the Morrison scheme presents slow growth in increased barometric pressure; however, the rain mixing ratio of the Goddard scheme increases quickly with increased barometric pressure. The difference in rain mixing ratio between them is 0.27 g/kg.

The solid-state hydrometeor in clouds mainly comprises snow crystal and ice crystal. The simulation of the snow mixing ratio on MAY15 is mainly distributed from 250 hPa to 700 hPa. The maximum simulated snow mixing ratios are at the barometric pressure of 500 hPa for the Morrison, WSM6, and Goddard schemes, while it is 450 hPa for Thompson. In these schemes, the snow mixing ratio simulation overtakes that of the rain mixing ratio. For the same cumulus convection scheme, the simulated snow mixing ratios of each microphysics scheme are in descending order: Goddard, Thompson, Morrison, and WSM6. Simultaneously, the ice mixing ratio is formed at higher altitudes,

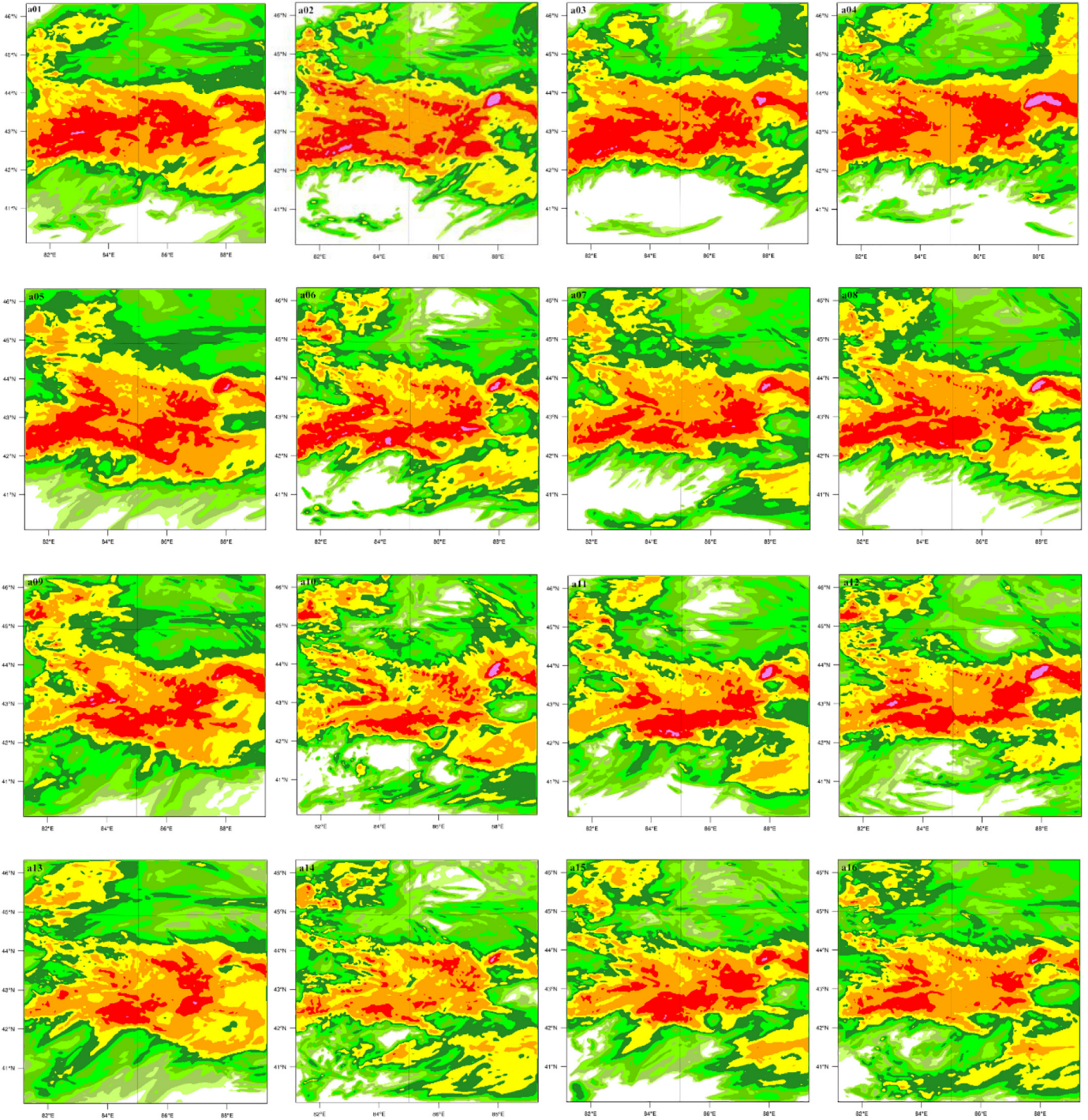


**Fig. 3.** Spatial patterns for the cumulative rainfall amounts of the MAY15(a1-a28).

where the simulated ice mixing ratio is mainly distributed from 250 hPa to 600 hPa. The maximum simulated ice mixing ratio is 300 hPa for Morrison and 350 hPa for WSM6; the maximum simulated ice mixing ratio is 400 hPa for Goddard. In the Goddard scheme, the ice mixing ratio simulation overtakes that of the rain mixing ratio. For the same cumulus scheme, the simulated ice mixing ratio of each microphysics scheme are ranked in descending order: WSM6, Morrison, Goddard, and Thompson. In the Thompson scheme, the simulated ice mixing ratio is negligible.

Moreover, In Fig. 6(b1-b4), the simulation of the snow mixing ratio on JUNE26 is mainly distributed from 250 hPa to 600 hPa; the simulated maximum snow mixing ratios is at the barometric pressure layer

of 500 hPa in the Morrison, WSM6, and Goddard schemes. The simulated snow mixing ratio overtakes that of the rain mixing ratio in these microphysics scheme. For the same cumulus convection scheme, the simulated snow mixing ratios of each microphysic scheme are in descending order: WSM6, Thompson, Morrison, and Goddard. Simultaneously, the ice mixing ratio is formed at higher altitudes, where the simulated ice mixing ratio is mainly distributed from 250 hPa to 600 hPa. The maximum simulated ice mixing ratio is 250 hPa for Morrison, while the maximum simulated ice mixing ratios are 350 hPa for WSM6 and Goddard schemes. The ice mixing ratio simulation overtakes that of the rain mixing ratio. For the same cumulus convection scheme, the simulated ice mixing ratios of each microphysics

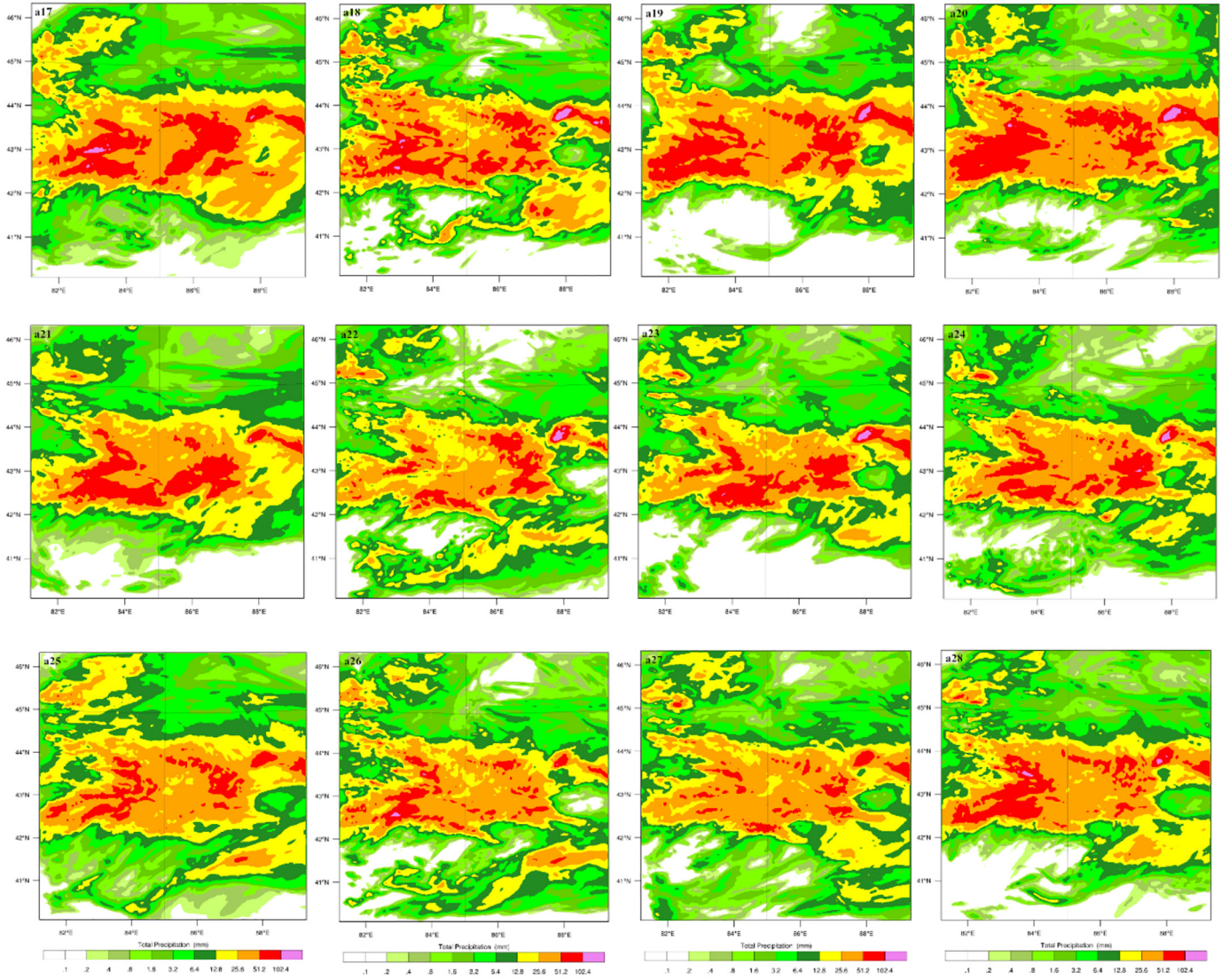


Fig. 3. (continued)

scheme are ranked in descending order: WSM6, Goddard, Morrison, and Thompson. In the Thompson scheme, the simulated ice mixing ratio is negligible.

## 5. Discussion

### 5.1. Impact on rainfall simulation by the four microphysics schemes

For a given cumulus scheme, an in-depth analysis of the simulation is conducted for the two case studies by four statistical indicators, namely BIAS, RMSE, MBE, and SD, to quantify the capabilities of the four microphysics schemes (Fig. 7, a-d).

The results show that the accumulated rainfall simulation of the four microphysics schemes is quite different. In detail, the accumulated rainfall simulated by the three microphysics schemes (Morrison, Goddard, and Thompson) is less than the actual rainfall amount observed. Furthermore, the Morrison, Thompson, and Goddard schemes are ranked in descending order according to RMSE, MBE, and SD scores. Moreover, the simulated rainfall amounts from the WSM6 scheme are slightly higher than the actual amounts, and the RMSE, MBE, and SD scores obtained from WSM6 are less than those from the Morrison, Goddard, and Thompson schemes.

For a given cumulus convection scheme, no matter what kinds of combinations are formed with microphysics schemes, there is a

significant difference in the rainfall simulations of each combination. This indicates that the important characteristic of microphysics properties is in the vertical structure. Specifically, the different mixing ratios of rainwater, ice crystal, cloud-water, and snow crystal are related to the microphysics schemes for the treatment of rainfall simulations (De Meij et al., 2018; Yin et al., 2019). The Morrison scheme can simulate the vertical water vapor profiles close to the actual observation by adding the cloud water change process within a sub-grid scale (Molthan, 2011); Zeng et al. (2008) found that the real state of ice water content in longer-term simulations could be achieved by adding different hydrometeors saturations within the Goddard scheme. According to some studies, the WSM6 scheme utilizes temperature-dependent inception parameters for snow- and ice mixing ratios (Hong et al., 2004); Additionally, the Thompson scheme can produce more snow ratio in contrast to the Morrison and WSM6 schemes, even though it possesses correction mechanisms for cloud water and ice crystals (Jankov et al., 2011).

Our results show that rainfall simulations in inland alpine areas rely heavily on the microphysics scheme. For instance, there are similar distributions of various hydrometeors simulated by different experimental setups with the same microphysics scheme on the barometric pressure layer (Fig. 6). Additionally, there are different distributions of the simulated mixing ratios of rainwater, ice crystal, cloud water, and snow crystal by different microphysics schemes on the barometric

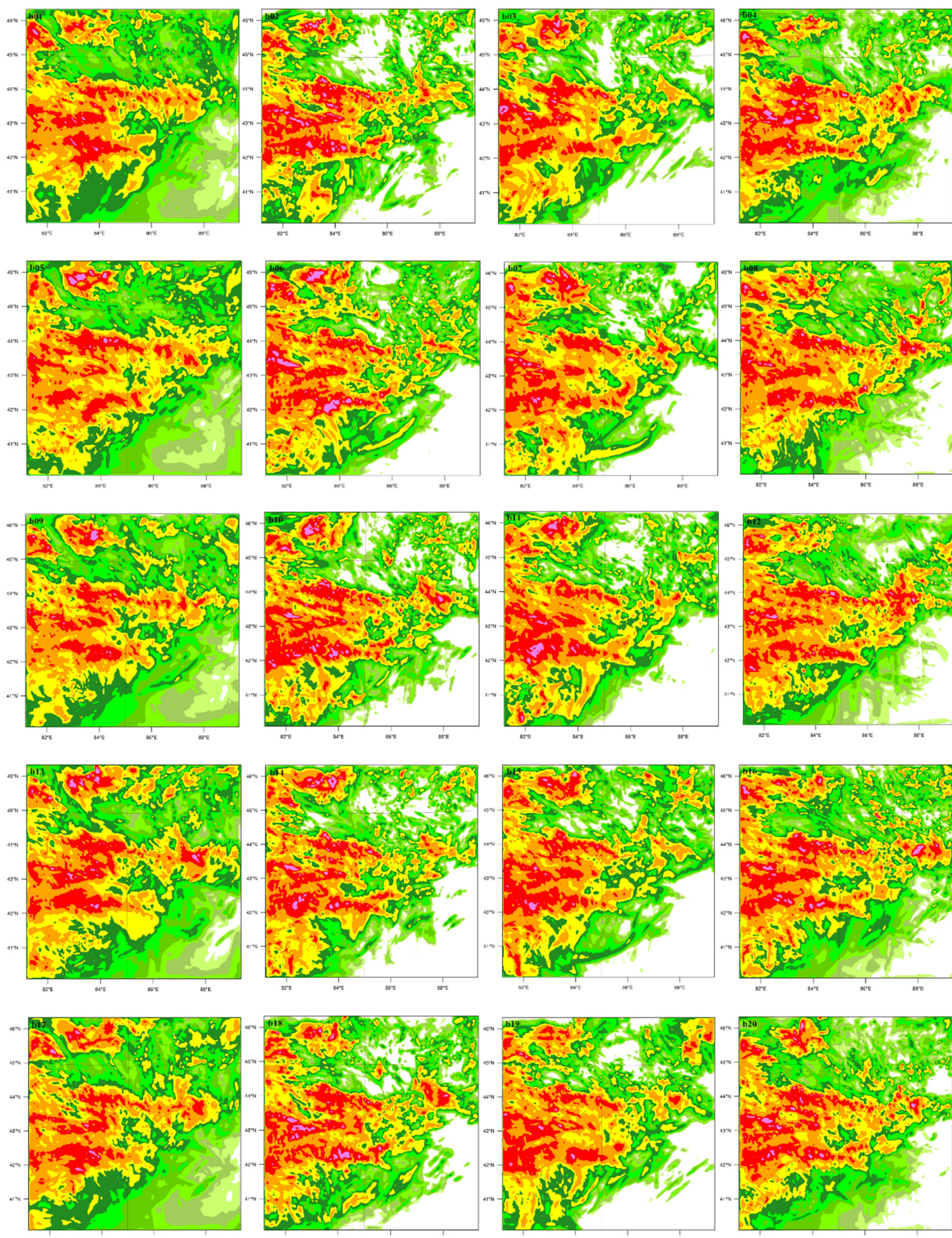


**Fig. 4.** Spatial patterns for the cumulative rainfall amounts of the JUNE26 (b1-b28).

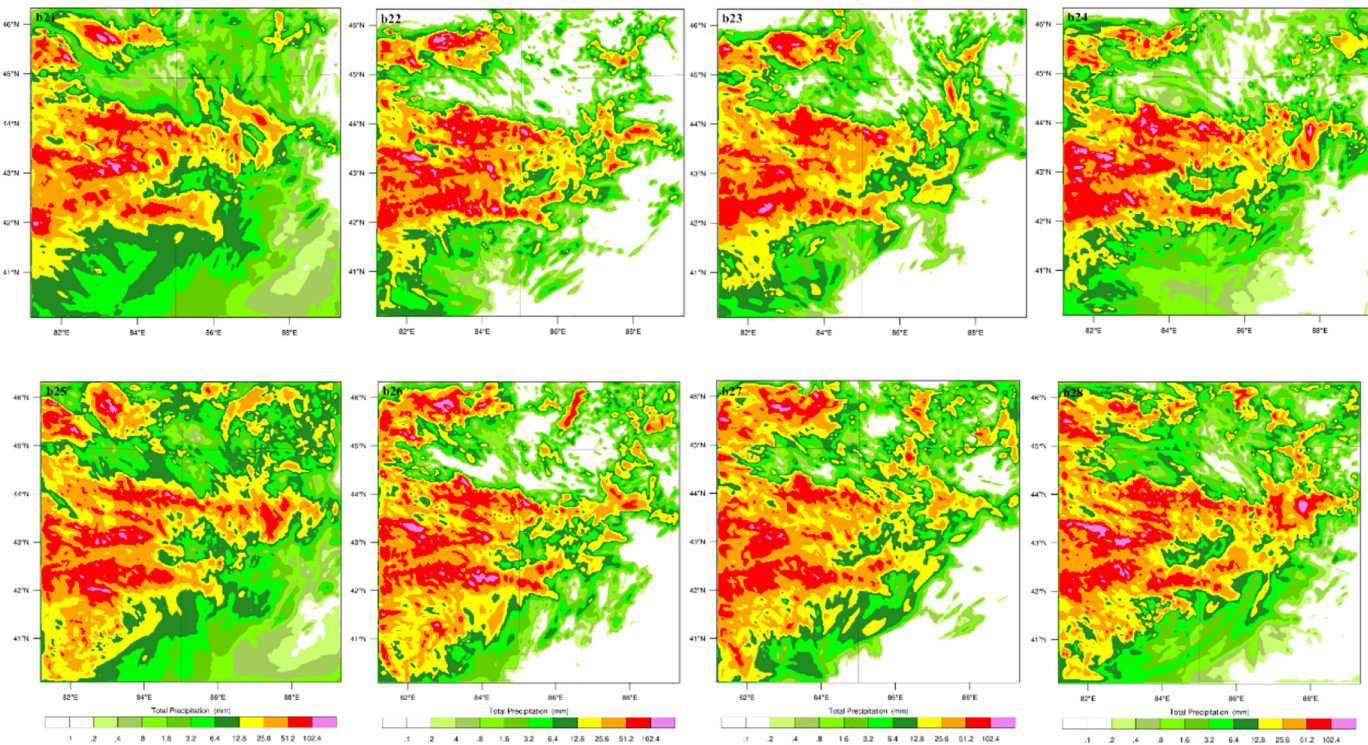


Fig. 4. (continued)

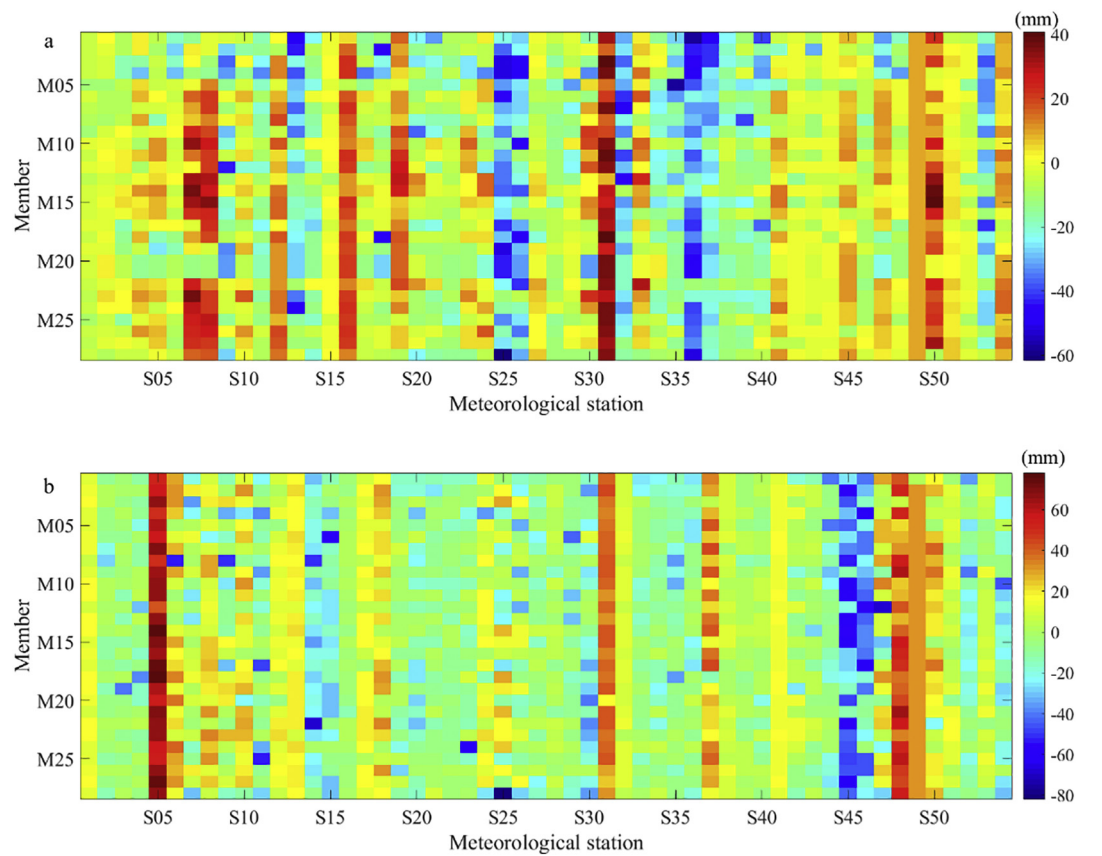
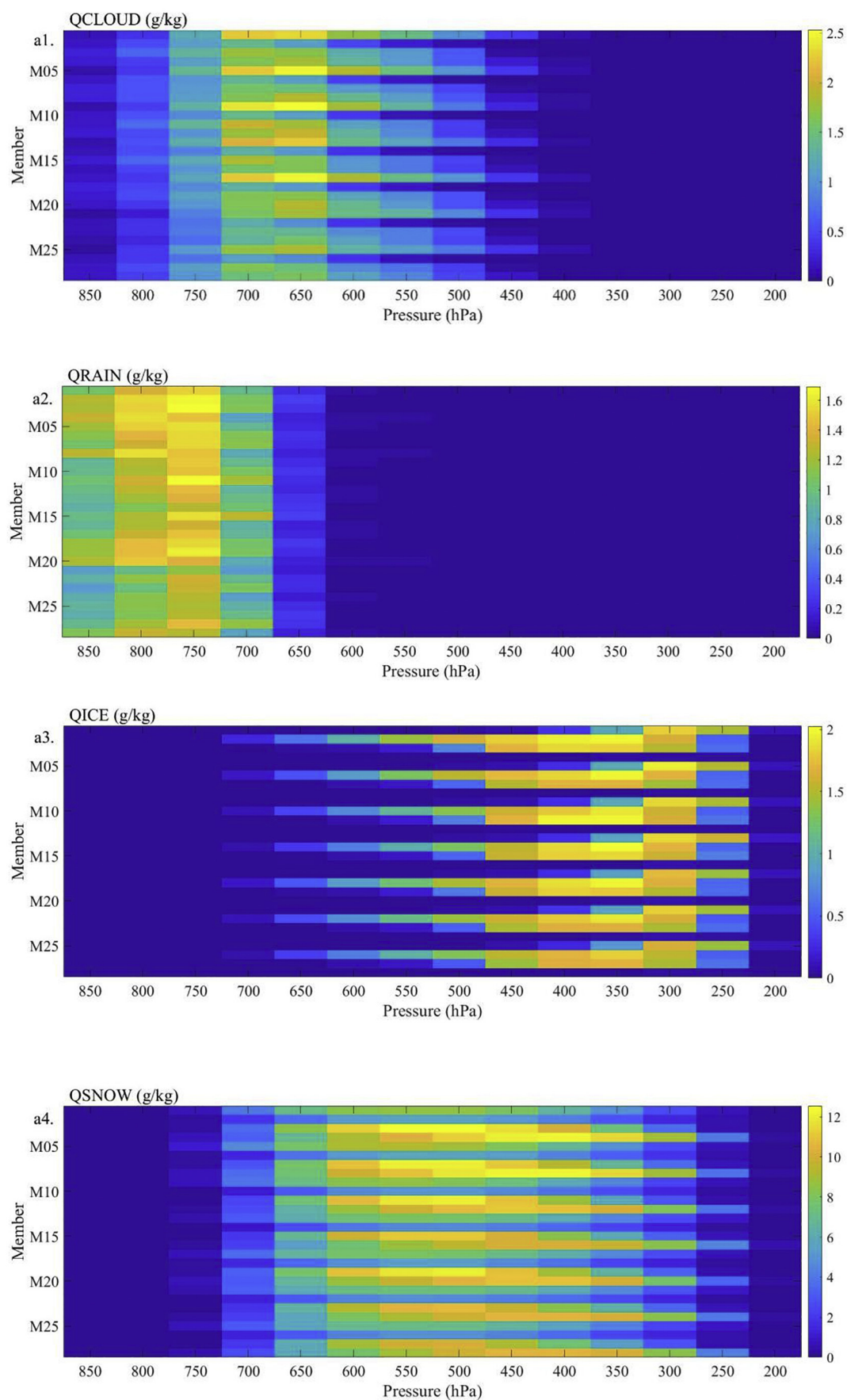


Fig. 5. The bias of the simulated and observed 48-h accumulated rainfall in every meteorological station with the 28 members of the physical combination (MAY15(a) and JUNE26(b)).



**Fig. 6.** Vertical profiles of 48-h average mass mixing ratios (g/kg) of hydrometeor variables simulation with the 28 members of the physical combination (MAY15(a1-a4) and JUNE26(b1-b4)).

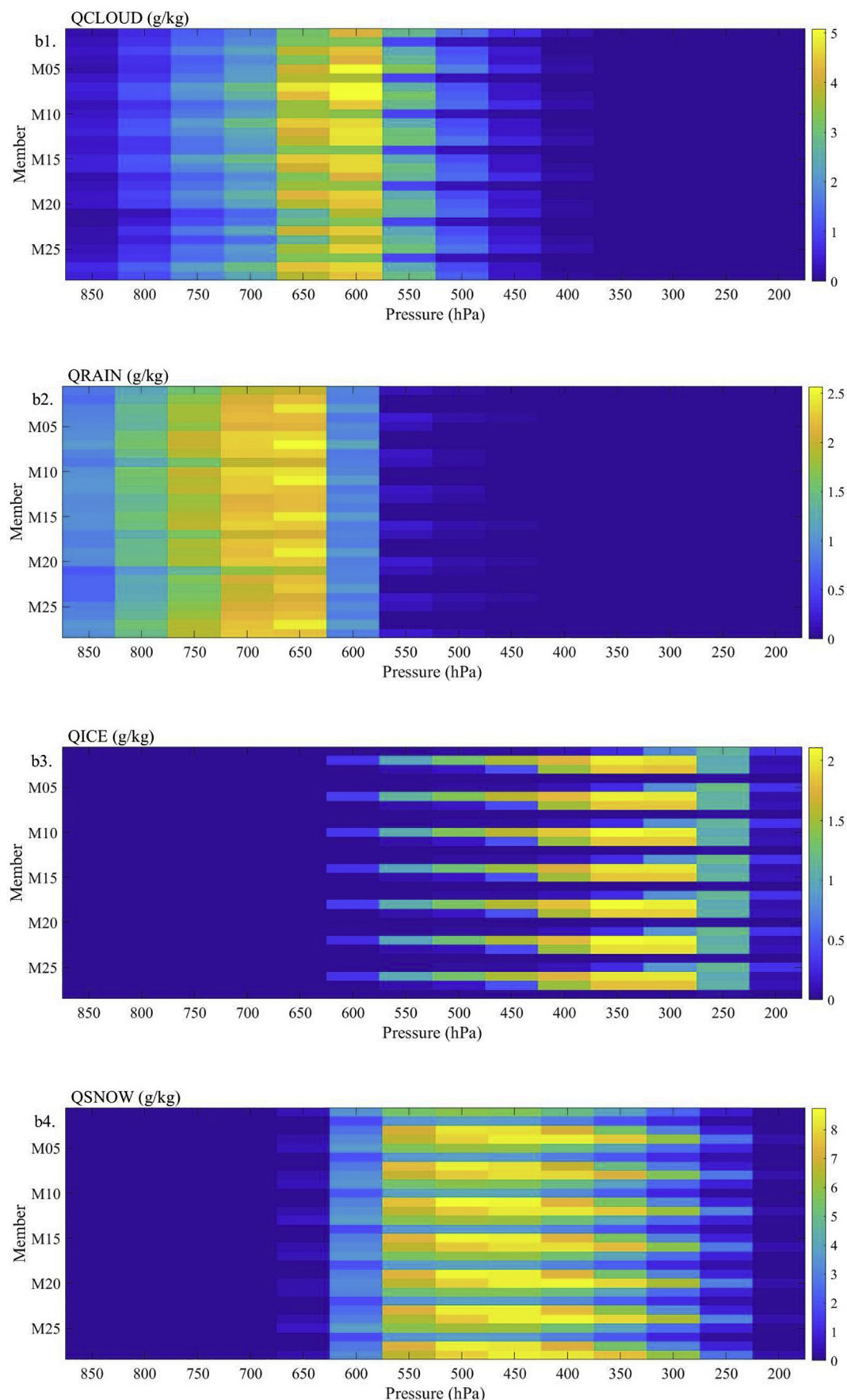


Fig. 6. (continued)

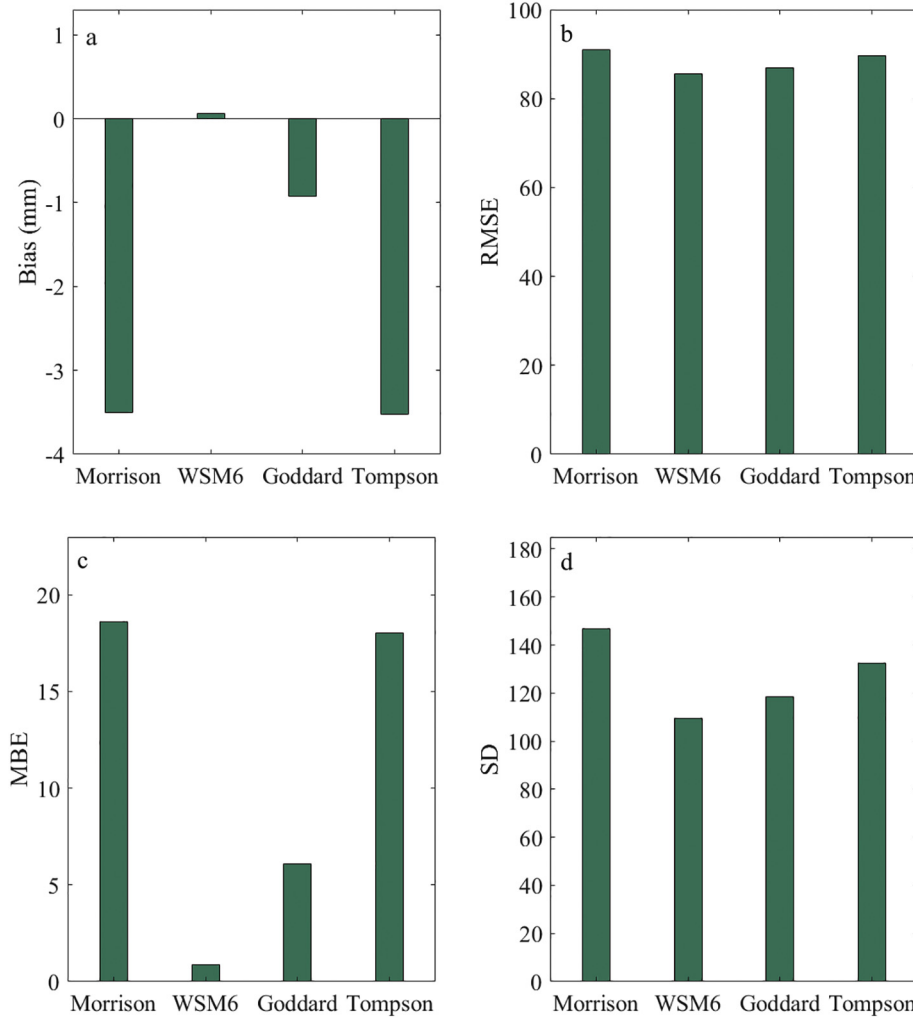


Fig. 7. (a)BIAS (mm) (b)RMSE (mm) (c)MBE (d)SD for the cumulative rainfall simulated by four microphysical schemes of the MAY15 and JUNE26.

pressure layer. Furthermore, combined with Figs. (4–5), the simulated rainfall distribution and amount in the central segment are closely related to that of the cloud water mixing ratio above 550 hPa and the rain mixing ratio above 650 hPa. Meanwhile, the cloud water and rain mixing ratios are larger when the simulated cumulative rainfall is obviously larger. However, there is no linear relationship between the simulated ice crystal mixing ratio and the accumulated rainfall in the study. This suggests that ice crystals may not directly affect rainfall.

Overall, the WSM6 more applicable to the central Tianshan Mountains because it can increase the simulated amount of ice crystals to reduce the simulated amount of snow crystals when the temperature is high (Hong et al., 2004). Unlike the other microphysics schemes, the simulation of this study shows that the snow crystal amount in the WSM6 scheme on the pressure layer of 300–600 hPa is about half that of the Morrison, Goddard, and Thompson schemes; the simulated rainfall zone and large value area in the WSM6 scheme are less than those of the other three microphysics schemes, indicating that larger rainfall is related to the higher concentration of the snow crystals produced by these microphysics schemes. Some researchers have also explored the WSM6's capacity for rainfall simulation. For instance, Tian et al. (2017) believe that the WSM6 is superior to the other micro-physics schemes with respect to its capacity for rainfall simulation in semi-humid and semi-arid catchments of Northern China. In other WSM6 scheme-driven simulations, some researchers shown that these simulations were close to the observational data-sets in Greece and Peru with complex topography (Morroni et al., 2017; Efstathiou et al., 2013;

Politi et al., 2018). Our results are similar to these studies, showing that the WSM6 scheme is suitable for cloud-resolving grids in terms of efficiency and theoretical backgrounds (Hong and Lim, 2006). In addition, it effectively avoids the over-extension of water vapor to generate other hydrometeors from adequate water vapor conditions.

### 5.2. Impact on rainfall simulation by the seven cumulus convection schemes

For a given microphysics scheme, the statistical results of the seven cumulus convection schemes are displayed for the rainfall simulation (Fig. 8, a-d). It can be seen from the BIAs, RMSE, MBE, and SD scores that the Grell-3 cumulus convection scheme is superior to the other cumulus convection schemes regarding heavy rainfall simulation in the central segment.

In detail, the accumulated rainfall amounts simulated by the five cumulus convection schemes from KF, BMJ, KF-CuP, GF, and GD are less than the actual rainfall amounts. Furthermore, KF, KF-CuP, BMJ, GF, and GD are ranked in descending order according to their RMSE, MBE, and SD scores. Moreover, the simulated rainfall amounts of the Grell-3 and New SAS schemes are higher than the actual amounts. The RMSE, MBE, and SD scores obtained from Grell-3 and New SAS schemes are less than that of the KF, BMJ, KF-CuP, GF, and GD schemes.

Specifically, the simulation of cumulative rainfall in inland alpine areas relies heavily on the cumulus convection schemes. For a given cumulus convection scheme, each combination with a microphysics scheme either overestimates or underestimates rainfall, which

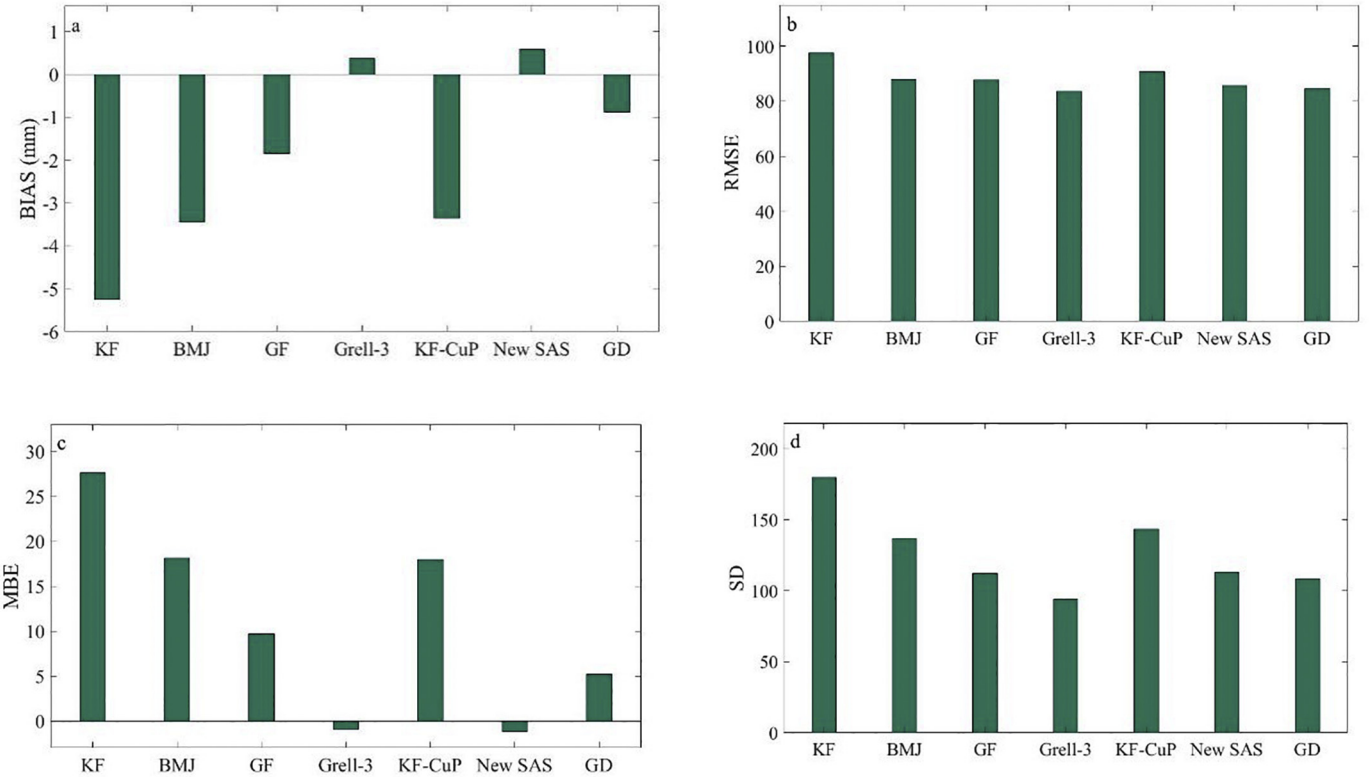


**Fig. 8.** (a)BIAS (mm) (b)RMSE (mm) (c)MBE (d)SD for the cumulative rainfall simulated by seven Cumulus schemes of the MAY15 and JUNE26.

illustrates that localized convection is rightfully within these cumulus convection schemes. In KF and KF-CuP schemes, the simple mass flux type is relevant to shallow convection, which is within the sub-grid scale convection of moist updrafts and downdrafts, including the effects of detrainment and entrainment (Kain, 2004; Kain and Fritsch, 1993; Berg et al., 2013a, b). It is noted that the KF-CuP outweighs KF in the presence of shallow convection (Qian et al., 2016). It replaces the default trigger function with a novel trigger function. The trigger function is related to the probability density function of temperature and humidity in the convective boundary layer (Berg and Stull, 2004); the BMJ scheme could simulate the shallow convection moisture profile on the ground that the entropy change is small and nonnegative (Janjic, 1994; Yu et al., 2011). Furthermore, with an ensemble of closure assumptions, the Grell-Dévényi scheme is a mass-flux type scheme with different entrainment and detrainment parameters for precipitation efficiency (Grell and Dévényi, 2002; Wu, 2012). The above-mentioned cumulus convection schemes effectively simulate the precipitation patterns of Eastern Africa, Central Africa, Western United States, and China. However, their accumulated rainfall was underestimated by the respective WRF model runs (Igri et al., 2018; Otieno et al., 2019; Yu et al., 2011). Without an appropriate adjustment process in convection, there are similar underestimated results in our study area.

The improved simulations from the New SAS, GF, and Grell-3 can be attributed to more active parameterized shallow convection, which is dependent on cloud layer moister and moist convection (Dong et al., 2016; Hierro et al., 2013). Grell-3, GF, and New SAS are introduced in this research since they overcome the drawbacks of KF, BMJ, and GD. Specifically, Grell-3 is more suitable for spatial resolutions less than 10 km because it spreads subsidence effects to neighboring grid columns, which is different from other cumulus schemes (Klich and Fuelberg, 2014). GF, an updated version of the Grell-Dévényi scheme, improves scale awareness to relax the assumption of traditional convection within the individual grid columns when the fractional area is covered by small convection clouds (Arakawa and Jung, 2011; Grell

and Freitas, 2014; Gao et al., 2017; Fowler et al., 2016). In the New SAS scheme, convective transport of horizontal momentum possesses mechanisms with compensated subsidence caused by warming and drying in a small area of the grid box (Igri et al., 2018; Kwon and Hong, 2017). Some researchers have explored these cumulus convection schemes' capacity for rainfall simulation. For instance, Li et al. (2011) found that the estimated summer rainfall amount in the Southeastern United States is higher than the actual amounts from the Grell-Dévényi and Grell-3 schemes; the Grell-3 scheme is suitable for rainfall simulation with spatial resolutions less than 10 km (Jeworrek et al., 2019a, b; Archer-Nicholls et al., 2015). Song and Sohn (2018) believe that New SAS works well in the Korean peninsula. Jeworrek et al., 2019a, b showed that GF has been the best-performing cumulus convection scheme for the two case studies in the US Southern Great Plains. However, our simulations are different from the above-mentioned studies. Only the Grell-3 is superior when it comes to capacity for accumulated rainfall simulation in the central Tianshan Mountains. It could be verified by lower reliance of Grell-3 on microphysics schemes, i.e. Grell-3 has shown low variability in combination with other microphysics schemes (Fig. 8, b-d). Additionally, Grell-3 results in less rainfall than other simulations in the high-intensity rainfall zone.

It should be noted that Grell-3 is more intricately redistributes convective flux air in columns, which leads to vertical updrafts from the boundary layer and downdrafts from the mid-level layer in complicated landform. Although there are various assumptions in such schemes for convective simulation, they are unable to resolve convection at the sub-grid scale.

### 5.3. Comparison with other simulations

This study shows that the microphysics and cumulus convection schemes for rainfall simulation in the Tianshan Mountains are less sensitive than those in Northern India, Southeast Bangladesh, and Eastern China (Tiwari et al., 2018a, b; Mohan et al., 2018; Di et al.,

2018; Deb et al., 2008). According to the statistical results pertaining to the observation values at the station, the error of the two selected HRs simulated by 28 combinations range from  $-12.67\text{--}5.48$  mm. The bias of HRs simulation in the Satluj Basin (most parts of Uttarakhand) of Northern India was found to range from 12 to 24 mm/day; the proportion of the bias for the HRs simulation in the mountainous region of Southeastern Bangladesh is approximately 25% (Tiwari et al., 2018a, b; Mohan et al., 2018). From the perspective of HR simulation in Eastern China, there is a large deviation between cumulative rainfall amounts from combinations and the actual rainfall amounts (Wang and Yu, 2013).

Since the central Tianshan Mountains belong to the arid, non-monsoon climate zone in Central Asia whose short spatio-temporal patterns synoptic systems leads to heavy rainfall, presenting obvious difference with the aforementioned ones. As a tangible description, the convergence of water vapor and unstable atmospheric junctions are not significantly linked to convective clouds and nimbostratus, i.e., the water vapor amount is deficient due to regional short-term adequate transmission of water vapor, which results in meso- and microscale weather systems without significant convection features.

#### 5.4. Limitations of microphysics and cumulus schemes in the numerical simulation of HRs

The microphysics and cumulus convection schemes exert great influence on the simulation of heavy rainfall (Politi et al., 2018). In particular, simulation accuracy cannot substantially decrease or increase with schemes changes, given that there are 28 combinations for simulated accumulated rainfall in the central Tianshan Mountains. To improve the accuracy of precipitation forecasts, some researchers propose optimized results through ensemble forecasts, i.e., ensemble members are adjusted by establishing weight from forecasting results (Singh et al., 2019; Fathi et al., 2019). In addition, other researchers adjust certain physical parameters in some WRF physical schemes to adapt the simulation cases (Di et al., 2018). However, this approach is not applicable to current conventional numerical weather forecasting. It is difficult to establish appropriate affiliate relationships due to deficient heavy rainfall observations with high spatio-temporal resolutions in the alpine region. Moreover, the accuracy of the model simulation is closely dependent to background field (Xu et al., 2009). Therefore, the forecasting accuracy can be improved by correcting the background field through data assimilation methods such as three-dimensional variational assimilation (Hou et al., 2013). However, this method cannot avoid the uncertainty of observation errors.

There are uncertainties in the precipitation data from every station site due to topographical diversity, altitude, slope, and aspect in the alpine region (Newman et al., 2019). Moreover, the observational stations and sites in the Tianshan Mountains are sparse and dispersed, i.e. 60% of the meteorological stations are established in the low mountain regions and the piedmont plain areas in the south and north slope of the Tianshan Mountains. Considering these reasons, this research is only focused on the applicability of the microphysics and cumulus convection schemes for cumulative rainfall. Future research should increase the number of precipitation observation stations in the alpine region and conduct ensemble forecast and variational assimilation for precipitation simulations.

## 6. Conclusion

According to 28 combinations in WRF3.9, numerical simulations are experimented on two HRs in the central Tianshan Mountains. This research further explores the influence of microphysics and convection mechanisms on rainfall simulation. The main conclusions are as follows:

(1) With simulations of POD, CSI, and FAR, WRF can be proved with

the capacity to simulate heavy rainfall in the central Tianshan Mountains. However, the combination of different microphysics and cumulus convection schemes exert significant influence on the simulations of falling zone and the rainfall amounts.

- (2) The WSM6 and the Grell-3 are applicable to the simulations of heavy rainfall in Tianshan Mountains due to certain advantages. WSM6 could adjust the content of snow and ice crystals with the temperature by effectively controlling the simulation quantity of snow crystals; with the temperature so as to effectively control the simulation quantity of snow crystals; Grell-3 could extend settlement effect to the adjacent grid, making it more suitable for rainfall simulation within a 10-km grid.
- (3) Whether the conclusions in this study is applicable to other rainfall intensity simulations in Tianshan mountainous regions remains to be further explored.

## Declaration of Competing Interest

The authors declare no conflict of interest.

## Acknowledgments

This study was supported by the National Natural Science Foundation of China (NSFC Grant U1703241, 41901087), the West Light Foundation of the Chinese Academy of Sciences (No. 2018-XBQNZ-B-012), and the Strategic Priority Research Program of the Chinese Academy of Sciences, the Pan-Third Pole Environment Study for a Green Silk Road (Pan-TPE) (No. XDA2004030202). The authors acknowledge Xinjiang Key Laboratory of Water Cycle and Water Utilization in Arid Zone for providing computing resources of Cluster Labrador for data processing. Moreover, the authors are grateful to the editor and anonymous expert reviewers for their professional and pertinent comments which are greatly helpful for further quality improvement of this paper.

## References

- Arakawa, A., Jung, J.H., 2011. Multiscale modeling of the moist-convective atmosphere - a review. *Atmos. Res.* 102 (3), 263–285.
- Archer-Nicholls, S., Lowe, D., Schultz, D.M., McFiggans, G., 2015. Aerosol-radiation-cloud interactions in a regional coupled model: the effects of convective parameterisation and resolution. *Atmos. Chem. Phys.* 15 (19), 27449–27499.
- Avolio, E., Federico, S., 2018. WRF simulations for a heavy rainfall event in southern Italy: Verification and sensitivity tests. *Atmos. Res.* 209, 14–35.
- Banks, R.F., Baldasano, J.M., 2016. Impact of WRF model PBL schemes on air quality simulations over Catalonia, Spain. *Sci. Total Environ.* 98–113.
- Berg, L.K., Stull, R.B., 2004. Parameterization of joint frequency distributions of potential temperature and water vapor mixing ratio in the daytime convective boundary layer. *J. Atmos. Sci.* 61, 813–828.
- Berg, L.K., Gustafson, W.I., Kassianov, E.I., Deng, L., 2013a. Evaluation of a modified scheme for shallow convection: Implementation of CuP and case studies. *Mon. Weather Rev.* 141 (1), 134–147.
- Berg, L.K., Gustafson, W.I., Kassianov, E.I., Deng, L.P., 2013b. Evaluation of a modified scheme for shallow convection: Implementation of CuP and case studies. *Mon. Weather Rev.* 141, 134–147.
- Budakoti, S., Singh, C., Pal, P.K., 2019. Assessment of various cumulus parameterization schemes for the simulation of very heavy rainfall event based on optimal ensemble approach. *Atmos. Res. Atmos. Res.* 218, 195–206.
- Burakowski, E.A., Ollinger, S.V., Bonan, G.B., Wake, C.P., Dibb, J.E., Hollinger, D.Y., 2016. Evaluating the Climate Effects of Reforestation in New England Using a Weather Research and Forecasting (WRF) Model Multiphysics Ensemble. *J. Clim.* 29 (14), 5141–5156.
- Cai, Y., Lu, X., Chen, G., Yang, S., 2018. Diurnal cycles of Mei-yu rainfall simulated over eastern China: Sensitivity to cumulus convective parameterization. *Atmos. Res.* 213, 236–251.
- Cannon, F., Carvalho, L.M., Jones, C., Norris, J., Bookhagen, B., Kiladis, G.N., 2017. Effects of Topographic Smoothing on the Simulation of Winter Precipitation in High Mountain Asia. *Journal of Geophysical Research* 122 (3), 1456–1474.
- Chawla, I., Osuri, K.K., Mujumdar, P.P., Niyogi, D., 2018. Assessment of the weather research and forecasting (WRF) model for simulation of extreme rainfall events in the upper Ganga Basin. *Hydrol. Earth Syst. Sci.* 22 (2), 1095–1117.
- Chen, S., Hu, J., Zhang, A., Min, C., Huang, C., Liang, Z., 2019. Performance of near real-time Global Satellite Mapping of Precipitation estimates during heavy precipitation events over northern China. *Theor. Appl. Climatol.* 135 (3–4), 877–891.

- Dasari, H.P., Salgado, R., 2015. Numerical modelling of heavy rainfall event over Madeira Island in Portugal: Sensitivity to different micro physical processes. *Meteorol. Appl.* 22 (1), 113–127.
- De Meij, A., Vinesa, J.F., Maupas, V., 2018. GHI calculation sensitivity on microphysics, land-and cumulus parameterization in WRF over the Reunion Island. *Atmos. Res.* 204, 12–20.
- Deb, S.K., Srivastava, T.P., Kishtawal, C.M., 2008. The WRF model performance for the simulation of heavy precipitating events over Ahmedabad during August 2006. *J. Earth Syst. Sci.* 117 (5), 589–602.
- Di, Z., Duan, Q., Wang, C., Ye, A., Miao, C., Gong, W., 2018. Assessing the applicability of WRF optimal parameters under the different precipitation simulations in the Greater Beijing Area. *Clim. Dyn.* 50 (5–6), 1927–1948.
- Diaz, J.P., Gonzalez, A., Exposito, F.J., Perez, J.C., Fernandez, J., Garciaadiez, M., Taima, D., 2015. WRF multi-physics simulation of clouds in the African region. *Q. J. R. Meteorol. Soc.* 14 (692), 2737–2749.
- Dong, W., Lin, Y., Wright, J.S., Ming, Y., Xie, Y., Wang, B., Luo, Y., Uang, W., Huang, J., Wang, L., Tian, L., Peng, Y., Xu, F., 2016. Summer rainfall over the southwestern Tibetan Plateau controlled by deep convection over the Indian subcontinent. *Nat. Commun.* 7 (1), 1–9.
- Efstathiou, G.A., Zoumakis, N.M., Melas, D., Lolis, C.J., Kassomenos, P., 2013. Sensitivity of WRF to boundary layer parameterizations in simulating a heavy rainfall event using different microphysical schemes. Effect on large-scale processes. *Atmos. Res.* 132, 125–143.
- Fathi, M., Azadi, M., Kamali, G., Meshkatee, A.H., 2019. Improving precipitation forecasts over Iran using a weighted average ensemble technique. *J. Earth Syst. Sci.* 128 (5), 133.
- Fowler, L.D., Skamarock, W.C., Grell, G.A., Freitas, S.R., Duda, M.G., 2016. Analyzing the Grell-Freitas convection scheme from hydrostatic to nonhydrostatic scales within a global model. *Mon. Weather Rev.* 144 (6), 2285–2306.
- Gallus, W.A., 1999. Eta simulations of three extreme precipitation events: Sensitivity to resolution and convective parameterization. *Weather Forecast.* 14, 405–426.
- Gao, Y., Leung, L.R., Zhao, C., Hagos, S., 2017. Sensitivity of U.S. summer precipitation to model resolution and convective parameterizations across gray zone resolutions. *J. Geophys. Res.* 122 (5), 2714–2733.
- Grell, G.A., Dévényi, D., 2002. A generalized approach to parameterizing convection combining ensemble and data assimilation techniques. *Geophys. Res. Lett.* 29 (14), 1–14.
- Grell, G.A., Freitas, S.R., 2014. A scale and aerosol aware stochastic convective parameterization for weather and air quality modeling. *Atmos. Chem. Phys.* 14 (10), 5233–5250.
- Hasan, M.A., Islam, A.K.M.S., 2018. Evaluation of microphysics and cumulus schemes of WRF for forecasting of Heavy Monsoon Rainfall over the Southeastern Hilly Region of Bangladesh. *Pure Appl. Geophys.* 175 (12), 4537–4566.
- Hierro, R., Pessano, H., Llamedo, P., de la Torre, A., Alexander, P., Odiard, A., 2013. Orographic effects related to deep convection events over the Andes region. *Atmos. Res.* 120, 216–225.
- Hong, S.Y., Dudhia, J., Chen, S.H., 2004. A revised approach to ice microphysical processes for the bulk parameterization of clouds and precipitation. *Mon. Weather Rev.* 132 (1), 103–120.
- Hong, S., Lim, J.J., 2006. The WRF Single-Moment 6-Class Microphysics Scheme (WSM6). *Asia-Pacific Journal of Atmospheric Sciences* 42 (2), 129–151.
- Hoose, C., Karrer, M., Barthlott, C., 2018. Cloud top phase distributions of simulated deep convective clouds. *J. Geophys. Res. Atmos.* 123 (18), 10–464.
- Hou, T., Kong, F., Chen, X., Lei, H., 2013. Impact of 3DVAR Data assimilation on the prediction of heavy rainfall over Southern China. *Adv. Meteorol.* 1–17.
- Hou, T., Kong, F., Chen, X., Lei, H., Hu, Z., 2015. Evaluation of radar and automatic weather station data assimilation for a heavy rainfall event in southern China. *Adv. Atmos. Sci.* 32 (7), 967–978.
- Huang, D., Gao, S., 2017. Impact of different cumulus convective parameterization schemes on the simulation of precipitation over China. *Tellus Ser. A Dyn. Meteorol. Oceanogr.* 69 (1), 1406264.
- Huang, Y., Wang, Y., Xue, L., Wei, X., Zhang, L., Li, H., 2020. Comparison of three microphysics parameterization schemes in the WRF model for an extreme rainfall event in the coastal metropolitan City of Guangzhou. *China. Atmos. Res.* 104939.
- Igri, P.M., Tanessong, R.S., Vondou, D.A., Panda, J., Garba, A., Mkankam, F.K., Kamga, A., 2018. Assessing the performance of WRF model in predicting high-impact weather conditions over Central and Western Africa: an ensemble-based approach. *Nat. Hazards* 93 (3), 1565–1587.
- Janjic, Z.I., 1994. The step-mountain eta coordinate model: further developments of the convection, viscous sublayer, and turbulence closure schemes. *Mon. Weather Rev.* 122 (5), 927–945.
- Jankov, I., Gallus, W.A., Segal, M., Shaw, B., Koch, S.E., 2005. The impact of different WRF model physical parameterizations and their interactions on warm season MCS rainfall. *Weather Forecast.* 2005 20 (6), 1048–1060.
- Jankov, I., Grasso, L.D., Sengupta, M., Neiman, P.J., Zupanski, D., Zupanski, M., Lindsey, D., Hillger, D.W., Birkenheuer, D.L., Brummer, R., Yuan, H., 2011. An evaluation of five ARW-WRF microphysics schemes using synthetic GOES imagery for an atmospheric river event affecting the California coast. *J. Hydrometeorol.* 12 (4), 618–633.
- Jeworrek, J., West, G., Stull, R., 2019a. Evaluation of cumulus and microphysics parameterizations in WRF across the Convective Gray Zone. *Weather Forecast.* 34 (4), 1097–1115.
- Jeworrek, J., West, G., Stull, R., 2019b. Evaluation of cumulus and microphysics parameterizations in WRF across the convective gray zone. *Weather Forecast.* 34 (4), 1097–1115.
- Kain, J.S., 2004. The Kain–Fritsch convective parameterization: an update. *J. Appl. Meteorol.* 43, 170–181.
- Kain, J.S., Fritsch, J.M., 1993. Convective parameterization for mesoscale models: the Kain–Fritsch scheme. The representation of cumulus convection in numerical models, *Meteor. Monogr.*, No. 24. Amer. Meteor. Soc. 165–170.
- Khodayar, S., Kalthoff, N., Kottmeier, C., 2018. Atmospheric conditions associated with heavy precipitation events in comparison to seasonal means in the western mediterranean region. *Clim. Dyn.* 51 (3), 951–967.
- Kim, J.H., Shin, D. Bin, Kummerow, C., 2013. Impacts of a priori databases using six WRF microphysics schemes on passive microwave rainfall retrievals. *J. Atmos. Ocean. Technol.* 30 (10), 2367–2381.
- Klich, C.A., Fuelberg, H.E., 2014. The role of horizontal model resolution in assessing the transport of CO in a middle latitude cyclone using WRF-Chem. *Atmos. Chem. Phys.* 609–627.
- Kwon, Y.C., Hong, S.Y., 2017. A mass-flux cumulus parameterization scheme across gray-zone resolutions. *Mon. Weather Rev.* 145 (2), 583–598.
- Li, W., Li, L., Fu, R., Deng, Y., Wang, H., 2011. Changes to the North Atlantic subtropical high and its role in the intensification of summer rainfall variability in the south-eastern United States. *J. Clim.* 24 (5), 1499–1506.
- Li, X.R., Ke, F., Entao, Y., 2019a. Hindcast of extreme rainfall with high-resolution WRF: model ability and effect of physical schemes. *Theor. Appl. Climatol.* 1–20.
- Li, J., Yang, L., Liu, W., Jiang, C., 2019b. Spatiotemporal distribution characteristics of mesoscale convective systems producing short-duration heavy rainfall over the Tianshan Mountain Area. *Adv. Meteorol.* 9090659.
- Li, Q., Yang, T., Zhang, F., Qi, Z., Li, L.H., 2019c. Snow depth reconstruction over last century: Trend and distribution in the Tianshan Mountains, China. *Glob. Planet. Chang.* 173, 73–82.
- Liu, J., Bray, M., Han, D., 2012. Sensitivity of the weather research and forecasting (WRF) model to downscaling ratios and storm types in rainfall simulation. *Hydrol. Process.* 26 (20), 3012–3031.
- Liu, Y., Li, L.H., Chen, X., Yang, J.M., Hao, J.S., 2018a. Spatial distribution of snow depth based on geographically weighted regression kriging in the Bayanbulak Basin of the Tianshan Mountains, China. *J. Mt. Sci.* 15 (1), 33–45.
- Liu, Y., Li, L.H., Chen, X., Zhang, R., Yang, J.M., 2018b. Temporal-spatial variations and influencing factors of vegetation cover in Xinjiang from 1982 to 2013 based on GIMMS-NDVI3g. *Glob. Planet. Chang.* 169, 145–155.
- Liu, D., Yang, B., Zhang, Y., Qian, Y., Huang, A., Zhou, Y., Zhang, L., 2018c. Combined impacts of convection and microphysics parameterizations on the simulations of precipitation and cloud properties over Asia. *Atmos. Res.* 212, 172–185.
- Miao, Y., Guo, J., Liu, S., Zhao, C., Li, X., Zhang, G., Ma, Y., 2018. Impacts of synoptic condition and planetary boundary layer structure on the trans-boundary aerosol transport from Beijing-Tianjin-Hebei region to Northeast China. *Atmos. Environ.* 181, 1–11.
- Mohan, P.R., Srinivas, C.V., Yesubabu, V., Baskaran, R., Venkatraman, B., 2018. Simulation of a heavy rainfall event over Chennai in Southeast India using WRF: sensitivity to microphysics parameterization. *Atmos. Res.* 210, 83–99.
- Molthan, A.L., 2011. Evaluating the Performance of Single and Double Moment Microphysics Schemes during a Synoptic-Scale Snowfall Event, AMS Conferences on Weather and Forecasting/Numerical Weather Prediction, Seattle, WA.
- Morroni, G.Y., Gironás, J., Caneo, M., Delgado, R., 2017. Using Weather Research and forecasting (WRF) model for extreme precipitation forecasting in an Andean region with complex topography. *Eur. Water* 59, 85–90.
- Mugume, I., Waiswa, D., Mesquita, M.D.S., Reuder, J., Basalirwa, C., Bamutaze, Y., Ayesiga, G., 2017. Assessing the performance of WRF model in simulating rainfall over western Uganda. *J. Climatol. Weather Forecast* 5 (1), 1–9.
- Muhammad Tahir, K., Yin, Y., Wang, Y., Babar, Z.A., Yan, D., 2015. Impact assessment of orography on the extreme precipitation event of July 2010 over Pakistan: a numerical study. *Adv. Meteorol.* 510417.
- Nasrollahi, N., Aghakouchak, A., Li, J., Gao, X., Hsu, K., Sorooshian, S., 2012. Assessing the impacts of different WRF precipitation physics in hurricane simulations. *Weather Forecast.* 27 (4), 1003–1016.
- Navale, A., Singh, C., Budakoti, S., Singh, S.K., 2020. Evaluation of season long rainfall simulated by WRF over the NWH region: KF vs. MSKF. *Atmos. Res.* 232, 104682.
- Newman, A.J., Clark, M.P., Longman, R.J., Giambelluca, T.W., 2019. Methodological intercomparisons of station-based gridded meteorological products: Utility, limitations, and paths forward. *J. Hydrometeorol.* 20 (3), 531–547.
- Nikolopoulos, E.I., Anagnostou, E.N., Hossain, F., Gebremichael, M., Borga, M., 2010. Understanding the scale relationships of uncertainty propagation of satellite rainfall through a distributed hydrologic model. *J. Hydrometeorol.* 11 (2), 520–532.
- Otieno, G., Mutemi, J.N., Opijah, F.J., Ogallo, L.A., Omondi, M.H., 2019. The sensitivity of rainfall characteristics to cumulus parameterization schemes from a WRF model. Part I: a case study over East Africa during wet years. *Pure Appl. Geophys.* 1–16.
- Patel, P., Ghosh, S., Kaginalkar, A., Islam, S., Karmakar, S., 2019. Performance evaluation of WRF for extreme flood forecasts in a coastal urban environment. *Atmos. Res.* 223, 39–48.
- Pennelly, C., Reuter, G., Flesch, T., 2014. Verification of the WRF model for simulating heavy precipitation in Alberta. *Atmos. Res.* 135, 172–192.
- Piciullo, L., Calvello, M., Cepeda, J.M., 2018. Territorial early warning systems for rainfall-induced landslides. *Earth-Sci. Rev.* 179, 228–247.
- Politi, N., Nastos, P.T., Sfetsos, A., Vlachogiannis, D., Dalezios, N.R., 2018. Evaluation of the AWR-WRF model configuration at high resolution over the domain of Greece. *Atmos. Res.* 208, 229–245.
- Pontoppidan, M., Reuder, J., Mayer, S., Kolstad, E.W., 2017. Downscaling an intense precipitation event in complex terrain: the importance of high grid resolution. *Tellus Ser. A Dyn. Meteorol. Oceanogr.* 69 (1), 1271561.
- Qian, Y., Yan, H., Berg, L.K., Hagos, S., Feng, Z., Yang, B., Huang, M., 2016. Assessing impacts of PBL and surface layer schemes in simulating the surface-atmosphere interactions and precipitation over the tropical ocean using observations from AMIE/

- DYNAMO. *J. Clim.* 29 (22), 8191–8210.
- Reder, A., Iturbide, M., Herrera, S., Rianna, G., Mercogliano, P., Gutiérrez, J.M., 2018. Assessing variations of extreme indices inducing weather-hazards on critical infrastructures over Europe—the INTACT framework. *Clim. Chang.* 148 (1–2), 123–138.
- Scaff, L., Prein, A.F., Li, Y., Liu, C., Rasmussen, R., Ikeda, K., 2019. Simulating the convective precipitation diurnal cycle in North America's current and future climate. *Clim. Dyn.* 1–14.
- Schirmer, M., Jamieson, B., 2015. Verification of analysed and forecasted winter precipitation in complex terrain. *Cryosphere* 9 (2), 587–601.
- Sikder, S., Hossain, F., 2016. Assessment of the weather research and forecasting model generalized parameterization schemes for advancement of precipitation forecasting in monsoon-driven river basins. *J. Adv. Model. Earth Syst.* 8 (3), 1210–1228.
- Singh, B., Cash, B., Kinter III, J.L., 2019. Indian summer monsoon variability forecasts in the north American multimodel ensemble. *Clim. Dyn.* 53 (12), 7321–7334.
- Song, H.J., Sohn, B.J., 2018. An Evaluation of WRF Microphysics Schemes for Simulating the Warm-Type Heavy rain over the Korean Peninsula. *Asia-Pacific. J. Atmos. Sci.* 54 (2), 225–236.
- Tian, J., Liu, J., Yan, D., Li, C., Yu, F., 2017. Numerical rainfall simulation with different spatial and temporal evenness by using a WRF multiphysics ensemble. *Nat. Hazards Earth Syst. Sci.* 17 (4), 563–579.
- Tiwari, S., Kar, S.C., Bhatla, R., 2018a. Dynamic downscaling over western Himalayas: impact of cloud microphysics schemes. *Atmos. Res.* 201, 1–16.
- Tiwari, S., Kar, S.C., Bhatla, R., 2018b. Dynamic downscaling over western Himalayas: impact of cloud microphysics schemes. *Atmos. Res.* 201, 1–16.
- Wang, W., Seaman, N.L., 1997. A comparison study of convective parameterization schemes in a mesoscale model. *Mon. Weather Rev.* 125 (2), 252–278.
- Wang, S., Yu, E., 2013. Simulation and projection of changes in rainy season precipitation over China using the WRF model. *Acta Meteorol. Sin.* 27 (4), 577–584.
- Wu, T., 2012. A mass-flux cumulus parameterization scheme for large-scale models: description and test with observations. *Clim. Dyn.* 38 (3–4), 725–744.
- Xu, J., Rugg, S., Byerle, L., Liu, Z., 2009. Weather forecasts by the WRF-ARW model with the gsi data assimilation system in the complex terrain areas of Southwest Asia. *Weather Forecast.* 24 (4), 987–1008.
- Xu, M., Kang, S., Wu, H., Yuan, X., 2018. Detection of spatio-temporal variability of air temperature and precipitation based on long-term meteorological station observations over Tianshan Mountains, Central Asia. *Atmos. Res.* 203, 141–163.
- Yang, L., Yang, Q., Liu, Y., 2014. Characteristics of the atmospheric moisture cycle over the TianShan mountains. *Clim. Environ. Res.* 19 (1), 107–116.
- Yao, J.Q., Li, M., Yang, Q., 2018. Moisture sources of a torrential rainfall event in the arid region of East Xinjiang, China, based on a Lagrangian model. *Nat. Hazards* 92 (1), 183–195.
- Yin, L., Ping, F., Mao, J., 2019. Impact of cloud microphysical processes on the simulation of a hailstorm in East China. *Atmos. Res.* 219, 36–56.
- Yu, E., Wang, H., Gao, Y., Sun, J., 2011. Impacts of cumulus convective parameterization schemes on summer monsoon precipitation simulation over China. *Acta Meteorol. Sin.* 25 (5), 581–592.
- Zeng, X., Tao, W.K., Lang, S., Hou, A.Y., Zhang, M., Simpson, J., 2008. On the sensitivity of atmospheric ensembles to cloud microphysics in long-term cloud-resolving model simulations. *J. Meteorol. Soc. Japan. Ser. II* 86, 45–65.
- Zhang, M., Luo, G., De Maeyer, P., Cai, P., Kurban, A., 2017. Improved atmosphericmodelling of the oasis-desert system in Central Asia using WRF with actual satellite products. *Remote Sens.* 9 (12), 1273.
- Zhou, Y., Mu, Z., 2018. Impact of different reanalysis data and parameterization schemes on WRF dynamic downscaling in the Ili Region. *Water* 10 (12), 1729.